

# *Suzaku* Observations of the Non-thermal Supernova Remnant HESS J1731–347

Aya Bamba<sup>1</sup>, Gerd Pühlhofer<sup>2</sup>, Fabio Acero<sup>3</sup>, Dmitry Klochkov<sup>2</sup>, Wenwu Tian<sup>4,5</sup>, Ryo Yamazaki<sup>1</sup>, Zhiyuan Li<sup>6</sup>, Dieter Horns<sup>7</sup>, Karl Kosack<sup>8</sup>, Nukri Komin<sup>9</sup>

## ABSTRACT

A detailed analysis of the nonthermal X-ray emission from the North-Western and Southern parts of the supernova remnant (SNR) HESS J1731–347 with *Suzaku* is presented. The shell portions covered by the observations emit hard and line-less X-rays. The spectrum can be reproduced by a simple absorbed power-law model with a photon index  $\Gamma$  of 1.8–2.7 and an absorption column density  $N_{\text{H}}$  of  $(1.0\text{--}2.1)\times 10^{22}$  cm<sup>-2</sup>. These quantities change significantly from region to region; the North-Western part of the SNR has the hardest and most absorbed spectrum. The Western part of the X-ray shell has a smaller curvature than North-Western and Southern shell segments. A comparison of the X-ray morphology to the Very High Energy (VHE) gamma-ray and radio images was performed. The efficiency of electron acceleration and emission mechanism in each portion of the shell are discussed. Thermal X-ray emission from the SNR was searched for but could not be detected at a significant level.

---

<sup>1</sup> Department of Physics and Mathematics, Aoyama Gakuin University 5-10-1 Fuchinobe Chuo-ku, Sagamihara, Kanagawa 252-5258, Japan

<sup>2</sup> Institut für Astronomie und Astrophysik, Universität Tübingen, Sand 1, D 72076 Tübingen, Germany

<sup>3</sup> Laboratoire Univers et Particules de Montpellier, Université Montpellier 2, CNRS/IN2P3, CC 72, Place Eugene Bataillon, F-34095 Montpellier Cedex 5, France

<sup>4</sup> National Astronomical Observatories, CAS, Beijing 100012, China

<sup>5</sup> Department of Physics & Astronomy, University of Calgary, Calgary, Alberta T2N 1N4, Canada

<sup>6</sup> Harvard-Smithsonian Center for Astrophysics, 60 Garden Street, Cambridge, MA 02138, USA

<sup>7</sup> Universität Hamburg, Institut für Experimentalphysik, Luruper Chaussee 149, 22761 Hamburg, Germany

<sup>8</sup> CEA Saclay, DSM/IRFU, 91191 Gif-Sur-Yvette Cedex, France

<sup>9</sup> Laboratoire d'Annecy-le-Vieux de Physique des Particules, Université de Savoie, CNRS/IN2P3, F-74941 Annecy-le-Vieux, France

*Subject headings:* acceleration of particles — ISM: individual (HESS J1731–347)  
— X-rays: ISM

## 1. Introduction

Supernova remnants (SNRs) are widely believed to be the main source of Galactic cosmic rays. Observationally, several SNRs are found to have X-ray synchrotron-emitting shells, and are therefore widely known as electron accelerators at least up to  $\sim$ TeV energies. Many of them are identified as young SNRs from the records of supernovae, expansion velocity, and their bright thermal X-rays (e.g. Cas A, Tycho, Kepler, SN 1006; Koyama et al. (1995); Bamba et al. (2005a)). However, the nature of the prominent non-thermal X-ray-emitting SNRs RX J1713–3946 and Vela Jr. is still largely unclear (Koyama et al. 1997; Slane et al. 2001; Bamba et al. 2005b). The very low level of radio synchrotron emission, the lack of thermal X-ray emission, and poor expansion velocity data have yielded only weakly constrained key parameters of the SNRs, such as age and nature of the progenitor star. Remarkably, these SNRs are bright Very High Energy (VHE) gamma-ray emitters compared with other young SNRs (Aharonian et al. 2004, 2005). Thus, they are strong particle accelerators, and it is important to understand the nature of this small class of sources, and especially the puzzling absence of thermal X-rays.

HESS J1731–347 has been discovered in the VHE Galactic plane survey performed with the H.E.S.S. telescopes (Aharonian et al. 2008). Tian et al. (2008) discovered a shell structure in archival radio data spatially coincident with the VHE source, and the source (also named G353.6–0.7) was hence considered to be a newly discovered SNR with associated VHE gamma-ray emission. Subsequently, deep VHE follow-up observations were performed (Abramowski et al. 2011) that established a clear VHE shell-like structure in agreement with the radio shell.

Based upon a possible association of the SNR with a nearby HII region, Tian et al. (2008) suggested that the object could have the same distance ( $3.2 \pm 0.8$  kpc), using a flat Galactic rotation curve model and the most recent estimates of the parameters by Eisenhauer et al. (2005). A lower limit of the distance comes from the clear correlation of the X-ray absorption column density with a molecular cloud structure at  $\sim 3$  kpc as seen in CO emission (Abramowski et al. 2011), suggesting that the cloud is in the foreground of or interacting with the SNR. This SNR has no GeV counterpart in the *Fermi* 2-year Point Source Catalog (Fermi-LAT collaboration 2011).

*XMM-Newton* and *Suzaku* observations towards the center and the East of this SNR show that X-ray emission from the shell is dominated by non-thermal emission (Acero et al. 2009; Tian et al. 2010). This suggests that HESS J1731–347 could be the third member of the SNR class characterized by pure non-thermal X-ray emission and comparable VHE gamma-ray luminosity. A sensitive search for thermal X-ray emission across the entire remnant is needed to confirm this hypothesis.

From spatially resolved X-ray synchrotron spectra, changes of particle acceleration conditions can be studied. Such variations have already been found in other SNRs such as RX J1713–3946, and were attributed to electron cooling over the distance from the acceleration site (Tanaka et al. 2008).

In this paper, we report on *Suzaku* observations (Mitsuda et al. 2007) of the western half of the SNR HESS J1731–347. The observation details are summarized in §2. A first analysis of the *Suzaku* X-ray data is presented in §3, the results of which are discussed in §4.

## 2. Observations and Data Reduction

*Suzaku* observed the center region of HESS J1731–347 on 2007 Feb. 23–24, and the North-Western and Southern regions on 2010 Feb. 17–19. The mapping consists of three pointings as listed in Table 1. Data reduction and analysis were made using HEADAS software version 6.9, version 2.5.16.28 of the processed data, and XSPEC version 12.6.0.

*Suzaku* has two active instruments, four X-ray Imaging Spectrometers (XIS0–XIS3; Koyama et al. 2007) each at the focus of an X-Ray Telescope (XRTs Serlemitsos et al. 2007) and a separate Hard X-ray Detector (HXD; Takahashi et al. 2007).

Only three XISs could be used subsequently due to a problem with XIS 2. XIS1 is a back-illuminated (BI) CCD, whereas the others are front-illuminated (FI). The XIS instruments were operated in normal full-frame clocking mode. Spaced-row charge injection (Nakajima et al. 2008; Uchiyama et al. 2009) was used in the later two observations (Table 1). We filtered out data acquired during passages through the South Atlantic Anomaly (SAA), with elevation angle to the Earth’s dark limb below  $5^\circ$ , or with elevation angle to the bright limb below  $25^\circ$  in order to avoid contamination by emission from the bright limb. The remaining exposure time for each observation is summarized in Table 1.

The HXD PIN was operated in normal mode. We filtered out data obtained during passages through the SAA, with elevation angle to the Earth’s limb below  $5^\circ$ , and cut off rigidity (COR) smaller than 8 GV. The exposure time for each observation is again listed

in Table 1. For the non-X-ray background (NXB) model, we adopted the LCFIT model by Fukazawa et al. (2009). The cosmic X-ray background (CXB) flux is estimated based on the *HEAO1* results (Boldt 1987), and treated as an additional background component.

### 3. Results

#### 3.1. X-ray images

Figure 1 shows 0.5–2.0 keV and 2.0–8.0 keV mosaic images obtained with the *Suzaku* XIS instruments. We used only XIS1 and XIS3 for image analysis, since a part of XIS0 showed a known anomaly (JX-ISAS-SUZAKU-MEMO-2010-01) and discriminated that region in the data process before deriving spectra. The vignetting has been corrected in each image using *xissim* (Ishisaki et al. 2007).

One can see clear shell-like structures in both images. The shell has a rather clumpy and bulged structure. The Western part of the X-ray shell has a smaller curvature than the North-Western and Southern shell segments. At the center of the remnant, emission from the point source XMMU J173203.3–344518 (Tian et al. 2008) is seen, which from its soft spectrum and its position has been classified as the central compact object (CCO) (Acero et al. 2009; Abramowski et al. 2011). Tian et al. (2010) noted that the source spectrum is also compatible with a magnetar hypothesis. A claim of X-ray pulsation with a period of  $\sim 1$  s using *XMM-Newton* data also led Halpern & Gotthelf (2010a) to speculate that XMMU J173203.3–344518 might be a magnetar candidate, but a subsequent dedicated search for pulsations using Chandra timing observations did not confirm the signal (Halpern & Gotthelf 2010b).

In Fig. 2, a false-color image of the remnant is shown. The image reveals that the North-Western part of this object is characterized by significantly harder emission compared with the other regions.

#### 3.2. Multiwavelength comparison

This SNR has a shell-like structure not only in X-rays but also in radio and VHE gamma-rays (Tian et al. 2008; Abramowski et al. 2011). The top panel of Figure 3 shows a comparison of the *Suzaku* data with a radio map at 1.4 GHz from the ATCA south Galactic Plane survey (Haverkorn et al. 2006). Both images show clumpy shell structures, and an overall good agreement with each other. The bottom panel of Fig. 3 shows a compari-

son of the *Suzaku* data with the VHE gamma-ray map derived from H.E.S.S. observations (Abramowski et al. 2011). At first glance, it looks as if there are differences in the extent of the VHE and X-ray emissions towards the North-West and West of the source, respectively. Those differences might however be attributed to the coarser angular resolution of the VHE data (0.06 deg., 68% containment radius) compared with the *Suzaku* X-ray data (half power diameter of  $\sim 2$  arcmin, Mitsuda et al. 2007). We refer to the result of Abramowski et al. (2011) that the radio and VHE radio profiles of the entire remnant match well when the radio data are blurred to VHE resolution.

To illustrate the potential difference between the X-ray and the VHE radial profiles, in Fig. 4 the 2–8 keV profile for a wedge towards the west is compared to the VHE profile derived from the entire remnant. Besides the difference in angular resolution, it is also not yet feasible with the current VHE statistics to restrict the VHE data to a similarly small region. Further VHE observations using e.g. the planned Cherenkov Telescope Array CTA (Actis et al. 2011) are needed to provide sufficient VHE photon statistics to permit morphological comparisons on such small angular scales.

### 3.3. Spectra below 10 keV

#### 3.3.1. Diffuse emission

In order to perform a spatially-resolved spectral study below 10 keV with XIS, we divided the X-ray map into several regions, as shown in Figure 1. The background regions were taken from source-free regions of the same observations.

As can be seen in Figure 5, all background-subtracted spectra are hard and show no evidence of line emission. We thus fitted the spectra with an absorbed power-law model. The absorption model includes the cross sections of Balucinska-Church & McCammon (1992) with solar abundance (Anders & Grevesse 1989). Auxiliary files for the effective area were produced with `xissimarfgen` (Ishisaki et al. 2007), using the observed images of the source regions as photon distribution data. For each region, the spectra of all available XIS detectors were fitted simultaneously. For some regions, less than three XIS spectra are available because the regions overlap with the damaged part of XIS0 or with calibration sources. Because of this, we allowed for a difference of the normalization between different XIS spectra, and adopted the best-fit normalization derived from XIS3 as final result, since any remaining contamination from calibration sources is smallest in XIS3 for the regions analysed. Figure 5 and Table 2 show our best-fit models and parameters with 90% errors. In each case the power-law fit was statistically acceptable.

Figure 8 shows the best-fit photon index (left) and column density (right) for all analysed regions of the SNR. The North-Western part of the shell has a significantly harder and more absorbed spectrum, compared with the rest of the covered remnant. On the other hand, differences between other individual regions are not significant when statistical and systematic errors (at low surface-brightness regions, see below) are taken into account.

In order to better constrain the spectral shape of the non-thermal emission, we combined several adjacent regions to three cardinal areas: regions 1, 4, and 5 to the North-West, regions 3 and 6 to the Center-East, and regions 8–13 to the South, respectively. All the three spectra were again fitted well with an absorbed power-law model without any spectral break. The spectra with the best-fit models and their best-fit parameters are shown in Fig. 5 and Tab. 2, respectively. As already seen from the individual spectra, also in the combined spectra there is a significant change in photon index across the remnant, with the hardest spectrum in the North-West, where also the absorption column density is significantly larger than in the other two areas.

As illustrated in Fig. 1, we used two apparently source-free regions to estimate the average background of the entire source region. Due to the position dependence of the Galactic Ridge X-Ray Emission (GRXE), that can be  $\sim 20\%$  contribution in this region (Uchiyama 2010), the spectral parameters of low surface brightness regions might be misestimated. In order to quantify this systematic error, we artificially varied the background by  $\pm 20\%$  in the fit of region 9, which has the lowest surface brightness of all regions analyzed. Indeed, the systematic error in this region is comparable with the statistical error:  $\Gamma = 3.2 (+0.5-0.5)_{\text{stat}}(+0.7-0.4)_{\text{sys}}$  and  $N_{\text{H}} = (2.5 (+0.7-0.6)_{\text{stat}}(+0.9-0.5)_{\text{sys}}) \times 10^{22} \text{ cm}^2$ . For the high surface brightness regions ( $> 0.8 \times 10^{-13} \text{ erg cm}^{-2}\text{s}^{-1}\text{arcmin}^{-2}$ , see Table 2) which are relevant for the evaluation of the spectral and absorption trends, the systematic errors are below the 90% statistical errors. Therefore, while the significance of the observed absorption and photon index trends indeed weakens, they are nevertheless significantly observed.

In a power-law spectrum, photon index and absorption column densities are correlated to some extent. To further verify that the change of  $\Gamma$  and  $N_{\text{H}}$  in the *Suzaku* data across the remnant is indeed significant, we compared the confidence contours of  $\Gamma$  and  $N_{\text{H}}$  in the three cardinal areas. The left panel of Fig. 7 confirms that the North-Western area has significantly harder emission and higher absorption than the other two areas, and the south area has the softest emission. Similar checks were also done for several individual regions; the right panel of Fig. 7 illustrates that region 5 indeed exhibits significantly harder and more absorbed emission than region 12.

To investigate whether the source emits thermal radiation, we searched for emission lines of thermally heated plasma on top of the continuum spectra, but could not identify

promising candidates. This applies to the spectra derived from individual regions, as well as to the combined spectra from the three cardinal areas discussed above. We also tested the possibility that the lineless spectra could come from a highly absorbed hot plasma with low ionization age instead of from a nonthermal electron plasma. For this purpose, we fitted the softest spectrum from region 9 which also has the highest absorption column density, with an absorbed non-equilibrium ionization plasma model (NEI model, Borkowski et al. 2001). Indeed, the fit is statistically acceptable with a reduced  $\chi^2$  of 47.2/39. The resulting temperature is however higher than  $\sim 2$  keV, with an ionization timescale of  $\sim 10^9$  s  $\text{cm}^{-3}$ . Same conclusion or result holds if several regions with soft spectra are combined, using e.g. regions with photon indices larger than 2.5 in the southern half, namely regions 7, 8, 9, 11, 12, and 13. Again, the NEI model reproduces the spectra well with a reduced  $\chi^2$  of 60.7/118, with similar parameters as in region 9 ( $kT > 2.4$  keV, ionization time scale less than  $\sim 2 \times 10^8$  s  $\text{cm}^{-3}$ ). Such parameters would require a very young SNR or a recent encounter of a fast shock with a dense region, e.g. in a wind bubble scenario. Since age and environment of HESS J1731–347 are not known, such an interpretation is formally not precluded. It is however more natural to assume that the spectra in these regions are dominated by nonthermal synchrotron emission, in agreement with the hard regions where a pure thermal interpretation is virtually excluded.

### 3.3.2. *Spectrum of XMMU J173203.3–344518*

The central source of the SNR, XMMU J173203.3–344518, is in the field of view of the Suzaku XISs only in the first Suzaku pointing (ObsID 401099010, 2007/02/23–24). A first analysis of that data from the object has already been published by Tian et al. (2010). The uncertainty of their analysis is from the combination of the relatively coarse angular resolution ( $\sim 2$  arcmin) of Suzaku and the contamination from the surrounding SNR emission. We therefore repeated the spectral extraction, adding systematic checks to verify the robustness of the spectral results.

We used a circular source extraction region of 2.5 arcmin radius centered on XMMU J173203.3–344518 for the spectral analysis, which encompasses  $\sim 90\%$  of all source photons (Serlemitsos et al. 2007). As nominal background region, we chose an annulus around the source with 3–4.5 arcmin radius.

As already known, the central source has a rather soft spectrum compared with the diffuse emission from the SNR. As the first assumption, an absorbed blackbody model and an absorbed power-law model were fit to the data. The fits are statistically unacceptable (reduced  $\chi^2$  of 388.8/304 or 443.8/304, respectively). We conclude that the spectrum has a

multi component emission.

Fitting with a blackbody plus a power-law component model or a two-temperature blackbody model, yields better results, with reduced  $\chi^2$  of 334.7/302 or 340.7/302. The best-fit parameters for the blackbody plus power-law model are consistent with the results by Tian et al. (2010). The photon index for the power-law component,  $4.7_{-0.5}^{+0.5}$ , is rather soft for magnetars and CCOs; we therefore used a two temperature blackbody model in this paper. We show the spectrum with the best-fit model in Fig. 6 and the best-fit parameters in Tab. 3.

The second component, on the other hand, could be the contamination of the SNR emission. To check this possibility, we also fitted the spectrum with absorbed power-law or blackbody model plus the spectrum of the region 3 as a contamination, which is in the vicinity of the central source. The normalization of the contamination component was treated to be a free parameter, whereas photon index and absorption column density are fixed to those for region 3 spectrum. The  $\chi^2$ /d.o.f. becomes 443.8/303 for the power-law case and 350.8/303 for the blackbody case. The latter case has similar  $\chi^2$ /d.o.f. as the multi-component models. It is found that the source spectrum can be well reproduced by a single blackbody model and the second component in the spectra could be just the contamination of the diffuse SNR emission. The best-fit parameters of the previous model are shown in Tab. 3.

### 3.4. Spectra above 10 keV

We also analysed the HXD PIN data-set to search for a signal from the source in the energy range above 10 keV. After background (NXB+CXB) subtraction, the remaining count rate in the 15–40 keV band in each observation is  $3.7 \pm 0.3 \times 10^{-2}$  cts s<sup>-1</sup> for OBSID=401099010,  $1.7 \pm 0.3 \times 10^{-2}$  cts s<sup>-1</sup> for OBSID=504031010, and  $2.3 \pm 0.3 \times 10^{-2}$  cts s<sup>-1</sup> for OBSID=504032010. This is 12.4%, 2.9%, and 7.9% of the NXB count rate in this band, respectively. The systematic NXB uncertainty is 3–5% (Fukazawa et al. 2009), i.e.  $\sim 1\text{--}1.5 \times 10^{-2}$  cts s<sup>-1</sup>, but the uncertainty could be larger when the observation duration is shorter than 1 day (Fukazawa et al. 2009) as is the case here. Ignoring for the moment this caveat, the first and third observation appear to display significant emission above instrumental and extragalactic backgrounds in the 15–40 keV background.

Before potentially being able to attribute the excess signal to HESS J1731–347, another background, the GRXE, has to be considered. Its level is difficult to estimate since it is rather faint above 10 keV and its measurement is contaminated by bright point sources. Revnivtsev (2003) revealed with *RXTE* that the GRXE in this region is a few % of the diffuse emission in



the Galactic center (GC) region. This result is consistent with results obtained with *GINGA* X-ray satellite (Yamauchi and Ebisawa, private communication). With HXD PIN, the GC diffuse emission was resolved to be  $4 \times 10^{-10}$  erg cm $^{-2}$ s $^{-1}$ deg $^{-2}$  in the 12–40 keV band, or  $\sim 0.5$  cnt s $^{-1}$  in the 10–40 keV band (Yuasa et al. 2008). Our count rate is roughly 10% of that in the GC region, thus the emission is marginally above the GRXE.

Since HXD has no spatial resolution, any point source in the field of view ( $\sim 0.5$  deg. FWHM for PIN) adds to the total count rate in the detector. First of all, the CCO, XMMU J173203.3–344518, is almost at the center of OBSID=401099010. However, its spectrum is very soft, well described by a thermal blackbody with temperature 0.5 keV (Acero et al. 2009; Tian et al. 2010; Abramowski et al. 2011), and does therefore not significantly contribute to the emission above 10 keV in the field.

To identify potential hard-band emitting sources, we compared the three *Suzaku* fields of view with the *INTEGRAL* Fourth IBIS/ISGRI Soft Gamma-ray Survey Catalog (Bird et al. 2010). As a result, we found 4U 1728–337, a low-mass X-ray binary, which is  $\sim 50$  arcmin away from the center of the SNR. The source is variable with a 40–70 keV flux of  $\sim (1-6) \times 10^{-10}$  ergs s $^{-1}$ cm $^{-2}$  (Claret et al. 1994). During our *Suzaku* observations, 4U 1728–337 was detected with the RXTE All Sky Monitor (ASM) with a count rate of a few cnts s $^{-1}$ . Converting this value into an on-axis HXD PIN count rate results in a rough count rate estimate of  $\sim 0.1-1$  cnts s $^{-1}$  in the 15–40 keV band. For the actual source location at the edge of the HXD PIN FOV the expected count rate is one order of magnitude smaller, i.e.  $\sim 0.01-0.1$  cnts s $^{-1}$ . Given that this count rate is at the same level as the measured excess, from our observations we cannot claim any detection of X-rays above 10 keV from HESS J1731–347. Further studies using forthcoming *ASTRO-H* (Takahashi et al. 2010) and/or *NuStar* (Harrison et al. 2010) are needed to confirm this.

### 3.5. Searching for coherent pulsations from the central compact object

X-ray pulsations in the range of 0.1–0.4 s have been detected from a few CCOs (Halpern & Gotthelf 2010c). On the other hand, magnetars typically exhibit pulsations in the range of 2–12 seconds. The fact that the claimed pulsation of  $\sim 1$  s (Halpern & Gotthelf 2010a) could not be confirmed (Halpern & Gotthelf 2010b) does not preclude pulsations from XMMU J173203.3–344518.

Below 10 keV, the time resolution of XIS is 8 s (Koyama et al. 2007), insufficient for a sensitive search for pulsations. Above 10 keV, HXD provides adequate time resolution (61  $\mu$ s), and systematic background effects are negligible when searching for coherent pulsations (Terada et al. 2008a,b). Hence, even though the source was not significantly detected

in the HXD spectral analysis, a pulsation search was still performed. However, no significant pulsations were found in the scanned period range of 0.1 s to 1000 s.

## 4. Discussion

### 4.1. Diffuse emission from SNRs

The detailed analysis of the *Suzaku* data revealed that the North-Western shell of HESS J1731–347 exhibits stronger absorption than the rest of the source. The same trend has already been observed with *XMM-Newton* (Abramowski et al. 2011). Actually, the statistics obtained with *Suzaku* permit to test smaller scales, but the two regions (4 and 9, see Fig. 8) that seem to deviate from the overall trend also have the lowest surface brightness, and further investigation is needed to verify the result.

Towards the North-West of the SNR lies the Galactic Plane. However, the increase of the X-ray absorption column density can most likely not be attributed to the average gas density increase towards the Galactic Plane, since the measured  $N_{\text{H}}$  ( $1.9\text{--}2.1 \times 10^{22} \text{ cm}^{-2}$ ) is in clear excess of the average expected absorption column density in this direction ( $1.2\text{--}1.3 \times 10^{22} \text{ cm}^{-2}$  (Dickey & Lockman 1990; Kalberla et al. 2005)). That value is in fact consistent with the overall column density measured towards the South-East of the source. Indeed, Abramowski et al. (2011) showed that the absorption column derived from the *XMM-Newton* Eastern coverage of the source is well correlated with molecular gas, the density of which is derived from CO observations towards that region. The question remains whether the SNR is located at a distance of  $\sim 3$  kpc and interacting with a dense molecular cloud identified through the CO measurement at that distance, or whether the source is in fact located behind the cloud. CO observations of higher excited states may be helpful to find shock-heated gas.

The non-uniformity of the measured X-ray photon indices might offer another clue to that question. In SNRs, hard synchrotron spectra such as the ones detected here are typically attributed to electrons acceleration in fast shocks (several thousand  $\text{km s}^{-1}$ ). The harder the spectrum, the higher the maximum particle energy and hence the higher the speed of the shock. A lower shock speed might indicate the presence of dense material into which the shock is propagating. However, in the observations presented here, the North-West, which displays the highest column densities, also shows the hardest photon indices (e.g., region 1 and 5 in Table 2), at odds with a cloud-interaction scenario. We therefore stress again that at present there is no observational implication of the SNR-molecular cloud interaction in the North-Western part, and that it is more likely that the absorbing material lies in front of

the source. Furthermore, the flat azimuthal VHE profile and the lack of correlation between the absorption column and X-ray surface brightness also indicate that the SNR may in fact not be interacting with the molecular cloud but rather that the source is located behind the cloud.

The accumulated unabsorbed X-ray flux in our analysed regions is  $2.3 \times 10^{-11}$  ergs  $\text{cm}^{-2}\text{s}^{-1}$  in the 2–10 keV band. For the entire remnant, using our *Suzaku* observations together with the *XMM-Newton* results (Abramowski et al. 2011), the total flux of the source in this band is approximately  $\sim 5 \times 10^{-11}$  erg  $\text{cm}^{-2}\text{s}^{-1}$ . The non-thermal X-ray luminosity  $L$  and the radius of the source  $R$  are estimated to  $L \sim 5 \times 10^{34}$  erg  $\text{s}^{-1} \times d_{3\text{kpc}}^2$  and  $R \sim 14$  pc  $\times d_{3\text{kpc}}$  ( $d_{3\text{kpc}} = d/(3 \text{ kpc})$ , where  $d$  is the distance to the remnant). For a distance of 3 kpc, these values are in rough agreement with the SNR radius vs. non-thermal X-ray luminosity relation of Nakamura et al. (2011). If this relation also holds for HESS J1731–347, then it is possible that the SNR is in fact very near (but still behind) the molecular cloud that is responsible for the strong X-ray absorption.

Typical photon indices in the soft X-ray band from young SNRs like RX J1713–3946 range between  $\sim 2.3$  and  $\sim 2.6$  (Koyama et al. 1997; Slane et al. 2001). In the North-West of HESS J1731–347,  $\Gamma$  is as small as  $\sim 1.8$ . The only SNR known so far which shows a comparable photon index is CTB 37B (Nakamura et al. 2009), though the spectral extraction in the region of interest was very complex and subject to systematic uncertainties. Recently, Takahashi et al. (2008) discovered that the synchrotron spectra of RX J1713–3946 have a spectral break in the hard X-ray band, and that the photon index below the break is quite hard ( $\sim 1.5$ ). A similar break was also found in SN 1006 (Bamba et al. 2008). We speculate that the hard spectra in the North-Western region of HESS J1731–347 with  $\Gamma \leq 2$  are of similar nature. The Western and Southern regions have softer X-ray spectra. The photon index of 2.3–3.0 is typical for synchrotron X-rays from SNR shells (Bamba et al. 2005a, for example). We note that the Western part of the X-ray shell has a smaller curvature than the North-Western and Southern shell segments. This area looks promising to evaluate whether the VHE emission here does follow this trend, or whether the VHE shell is compatible with the larger average shell radius as the images seem to indicate (see Fig. 3). Such differences could be indicative of shock-cloud interaction and might provide important clues of shock-accelerated protons in SNRs: The X-rays trace the shock which has slowed down due to the encounter with a molecular cloud, while high energy protons have partially escaped the shock and are primarily emitting VHE  $\gamma$ -rays in the dense molecular cloud material. Similar phenomena are seen in W28 north-eastern shell (Nakamura 2011) and G359.1–0.5 (Bamba et al. 2009). As discussed earlier in this paper, the available VHE statistics are presumably not sufficient for such a test at this point of time. Also, the coverage of the X-ray emission in this particular area should be extended towards the West to pin-point the

outermost X-ray boundary here.

In several SNRs, synchrotron X-ray spectra are softer in downstream regions than regions close to the shock, e.g. in SN 1006 (Rothenflug et al. 2004) or in Tycho’s SNR (Cassam-Chenaï et al. 2007). Within the still limited *Suzaku* coverage of HESS J1731–347, however, no systematic trend could be found in the photon indices when comparing regions which are apparently shock-dominated with regions closer to the center of the remnant.

#### 4.2. XMMU J173203.3–344518

The spectrum of the central source XMMU J173203.3–344518 has at least one temperature blackbody component. If the hard component is represented by a power-law, the best-fit photon index, 4.7 (4.2–5.2), is not compatible with the hard tails usually detected in magnetars (c.f., Enoto et al. 2010). Moreover, the best-fit absorption column of  $2.5 (2.2–2.7) \times 10^{22} \text{ cm}^2$  significantly exceeds the values measured from the diffuse emission of the SNR. We therefore adopt in the following the two temperature blackbody model for the emission from this source.

Assuming that the distance to this source is 3 kpc, the radius of the emitting region is 2.2 (1.4–4.4) km for the low  $kT$  component ( $\equiv R_{\text{LT}}$ ) and 0.6 (0.2–0.8) km for the high  $kT$  component ( $\equiv R_{\text{HT}}$ ), respectively, i.e. the radiation is emitted from localized spots on the neutron star surface.

Although no flare has been detected from XMMU J173203.3–344518, it is instructive to compare the spectral results to flare spectra of soft gamma-ray repeaters (SGRs). These are well reproduced by two temperature blackbody models, and the radii of the two components has a positive correlation of  $R_{\text{HT}}^2/R_{\text{LT}}^2 \sim 0.03–0.4$  (Nakagawa et al. 2007). For XMMU J173203.3–344518, the ratio is 0.06, consistent with the above relation. Therefore, although the best-fit temperatures of both components are lower than flares, it is suggestive to interpret the emission from XMMU J173203.3–344518 in a magnetar scenario. Nevertheless, while a magnetar nature of XMMU J173203.3–344518 is possible, it clearly cannot be excluded, that the source is a CCO associated with the supernova remnant. Such objects are typically found in young SNRs and characterized by soft black body-like emission with  $kT \simeq 0.5 \text{ keV}$  and a lack of variability (except pulsations with periods below one second detected in some cases). The spectrum of one such object, PSR J1852+0040 — a confirmed CCO in SNR Kes 79, has also been fitted with a two-component black body ( $kT = 0.3$  and  $0.52 \text{ keV}$ ), as reported by Halpern & Gotthelf (2010a).

On the other hand, the harder component can be just contamination of the diffuse

SNR emission. The source spectrum in this case,  $\sim 0.5$  keV blackbody, is also typical for CCOs. Further detailed observations with good spatial resolution and statistics are needed to confirm the nature of this source.

We thank the anonymous referee for the useful comments. We thank all members of the *Suzaku* team who kindly scheduled these observations. We also thank S. Yamauchi and K. Ebisawa for the helpful comments on the GXRE, and Y. Fukazawa, T. Mizuno, and Y. Terada for the help of HXD analysis, and S. Terada for the help of writing this paper. This work was supported in part by Grant-in-Aid for Scientific Research of the Japanese Ministry of Education, Culture, Sports, Science and Technology (MEXT) of Japan, No. 22684012 (A. B.) and No. 21740184 (R. Y.). W.W.T. acknowledges support from NSFC, BeiRen Program of the CAS, and the 973 Program (2012CB821800).

## REFERENCES

- Abramowski, A., et al. (H.E.S.S. collaboration) 2011, *A&A*, 531, A81
- Acerro, F., Pühlhofer, G., Klochkov, D., Komin, N., Gallant, Y., Horns, D., Santangelo, A., & for the H. E. S. S. Collaboration 2009, arXiv:0907.0642
- Actis, M., Agnetta, G., Aharonian, F., et al. 2011, *Experimental Astronomy*, 32, 193
- Aharonian, F. A., et al. 2004, *Nature*, 432, 75
- Aharonian, F., et al. 2005, *A&A*, 437, L7
- Aharonian, F., et al. 2008, *A&A*, 477, 353
- Anders, E., & Grevesse, N. 1989, *Geochim. Cosmochim. Acta*, 53, 197
- Bamba, A., Yamazaki, R., Yoshida, T., Terasawa, T., & Koyama, K. 2005a, *ApJ*, 621, 793
- Bamba, A., Yamazaki, R., & Hiraga, J. S. 2005b, *ApJ*, 632, 294
- Bamba, A., Fukazawa, Y., Hiraga, J. S., et al. 2008, *PASJ*, 60, 153
- Bamba, A., Yamazaki, R., Kohri, K., Matsumoto, H., Wagner, S., Pühlhofer, G., & Kosack, K. 2009, *ApJ*, 691, 1854
- Bird, A. J., et al. 2010, *ApJS*, 186, 1
- Balucinska-Church, M., & McCammon, D. 1992, *ApJ*, 400, 699

- Borkowski, K. J., Lyerly, W. J., & Reynolds, S. P. 2001, *ApJ*, 548, 820
- Boldt, E. 1987, *Observational Cosmology*, 124, 611
- Cassam-Chenaï, G., Hughes, J. P., Ballet, J., & Decourchelle, A. 2007, *ApJ*, 665, 315
- Claret, A., et al. 1994, *ApJ*, 423, 436
- Dickey, J. M., & Lockman, F. J. 1990, *ARA&A*, 28, 215
- Eisenhauer, F., et al. 2005, *ApJ*, 628, 246
- Enoto, T., Nakazawa, K., Makishima, K., et al. 2010, *ApJ*, 722, L162
- Fermi-LAT collaboration, 2011, submitted to *ApJS*(arXiv:1108.1435)
- Fukazawa, Y., et al. 2009, *PASJ*, 61, 17
- Halpern, J. P., & Gotthelf, E. V. 2010, *ApJ*, 710, 941
- Halpern, J. P., & Gotthelf, E. V. 2010b, *ApJ*, 725, 1384
- Halpern, J. P., & Gotthelf, E. V. 2010c, *ApJ*, 709, 436
- Harrison, F. A., Boggs, S., Christensen, F., et al. 2010, *Proc. SPIE*, 7732, 77320S-77320S-8
- Haverkorn, M., Gaensler, B. M., McClure-Griffiths, N. M., Dickey, J. M., & Green, A. J. 2006, *ApJS*, 167, 230
- Ishisaki, Y., et al. 2007, *PASJ*, 59, 113
- Kalberla, P. M. W., Burton, W. B., Hartmann, D., Arnal, E. M., Bajaja, E., Morras, R., Pöppel, W. G. L. 2005, *A&A*, 440, 775
- Koyama, K., Petre, R., Gotthelf, E.V., Hwang, U., Matura, M., Ozaki, M., & Holt S. S. 1995, *Nature*, 378, 255
- Koyama, K., Kinugasa, K., Matsuzaki, K., Nishiuchi, M., Sugizaki, M., Torii, K., Yamauchi, S., & Aschenbach, B. 1997, *PASJ*, 49, L7
- Koyama, K. et al. 2007, *PASJ*, 59, S23
- Mitsuda, K., et al. 2007, *PASJ*, 59, 1
- Nakagawa, Y. E., Yoshida, A., Hurley, K., et al. 2007, *PASJ*, 59, 653

- Nakajima, H. et al. 2008, PASJ, 60, S1
- Nakamura, R., Bamba, A., Ishida, M., Nakajima, H., Yamazaki, R., Terada, Y., Pühlhofer, G., & Wagner, S. J. 2009, PASJ, 61, 197
- Nakamura, R., 2010, Ph.D. thesis
- Nakamura, R., Bamba, A., Dotani, T., et al. 2011, arXiv:1112.0822
- Revnivtsev, M. 2003, A&A, 410, 865
- Rothenflug, R., Ballet, J., Dubner, G., Giacani, E., Decourchelle, A., & Ferrando, P. 2004, A&A, 425, 121
- Serlemitsos, P. et al. 2007, PASJ, 59, S9
- Slane, P., Hughes, J. P., Edgar, R. J., Plucinsky, P. P., Miyata, E., Tsunemi, H., & Aschenbach, B. 2001, ApJ, 548, 814
- Takahashi, T. et al. 2007, PASJ, 59, S35
- Takahashi, T., et al. 2008, PASJ, 60, 131
- Takahashi, T., Mitsuda, K., Kelley, R., et al. 2010, Proc. SPIE, 7732, 77320Z-77320Z-18
- Tanaka, T., et al. 2008, ApJ, 685, 988
- Terada, Y., et al. 2008a, PASJ, 60, 25
- Terada, Y., Hayashi, T., Ishida, M., et al. 2008b, PASJ, 60, 387
- Tian, W. W., Leahy, D. A., Haverkorn, M., & Jiang, B. 2008, ApJ, 679, L85
- Tian, W. W., Li, Z., Leahy, D. A., Yang, J., Yang, X. J., Yamazaki, R., & Lu, D. 2010, ApJ, 712, 790
- Uchiyama, H., et al. 2009, PASJ, 61, 9
- Uchiyama, H. 2010, Ph.D. thesis, Kyoto University
- Yuasa, T., et al. 2008, PASJ, 60, 207

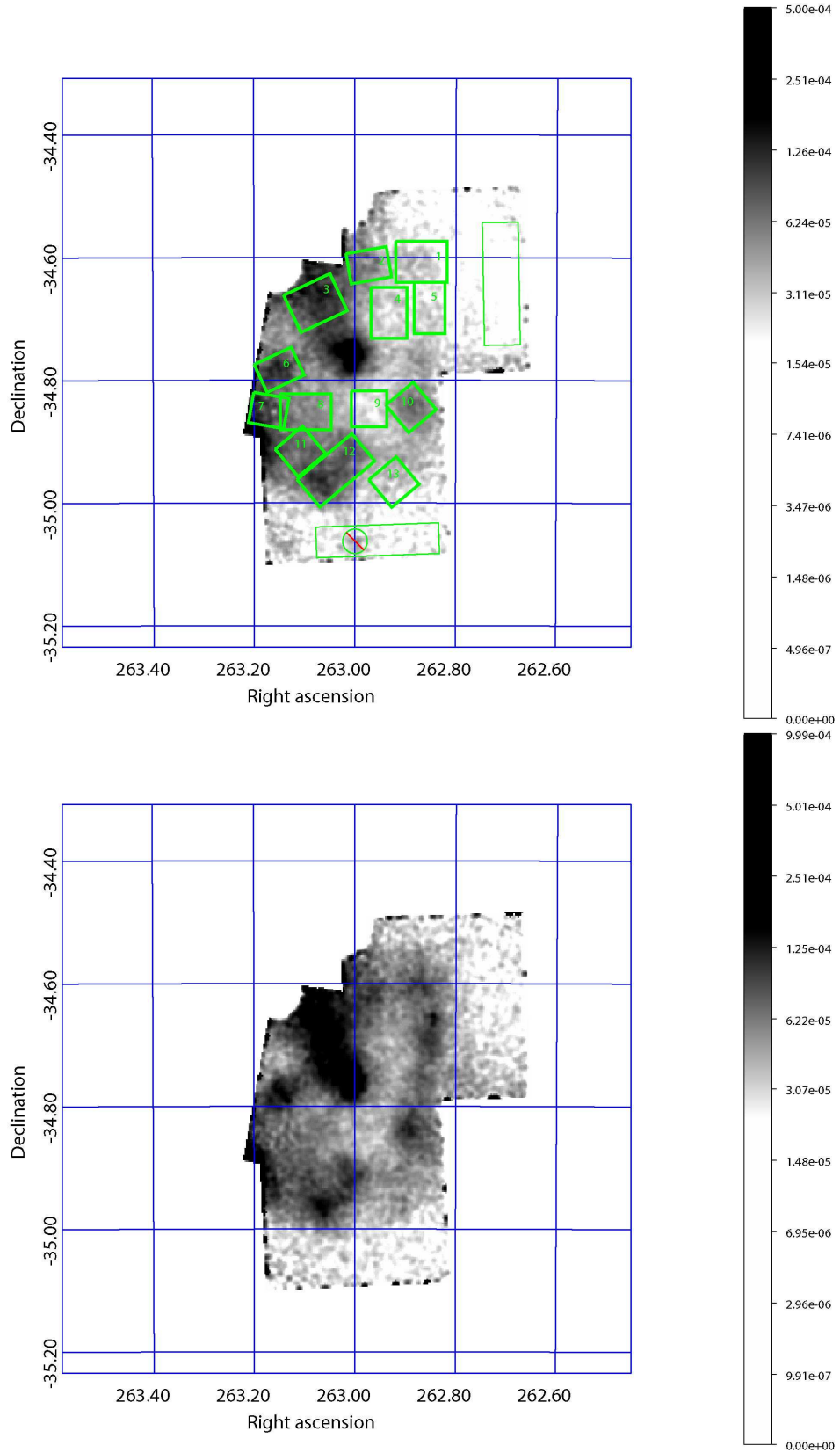


Fig. 1.— *Suzaku* XIS intensity maps of the North-Western, Western, and Southern regions of HESS J1731–347 in the 0.5–2.0 keV (top) and 2.0–8.0 keV (bottom) bands. The image is binned with 4 arcsec and smoothed with a two dimensional Gaussian of  $\sigma = 12$  arcsec.



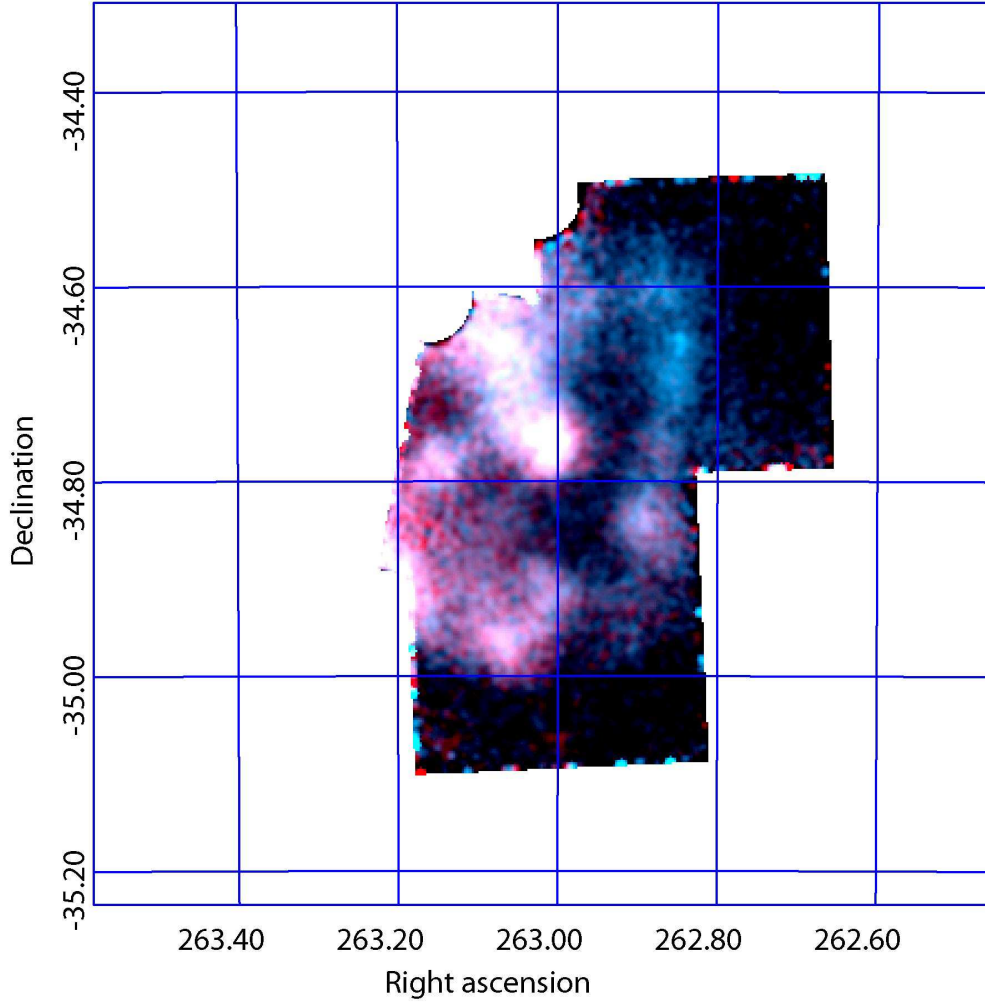


Fig. 2.— A false-color representation of the HESS J1731–347 North-Western, Western, and Southern regions. Red and blue correspond to 0.5–2.0 keV and 2.0–8.0 keV X-rays, respectively. The image is binned with 4 arcsec and smoothed with a two-dimensional Gaussian of  $\sigma = 12$  arcsec.

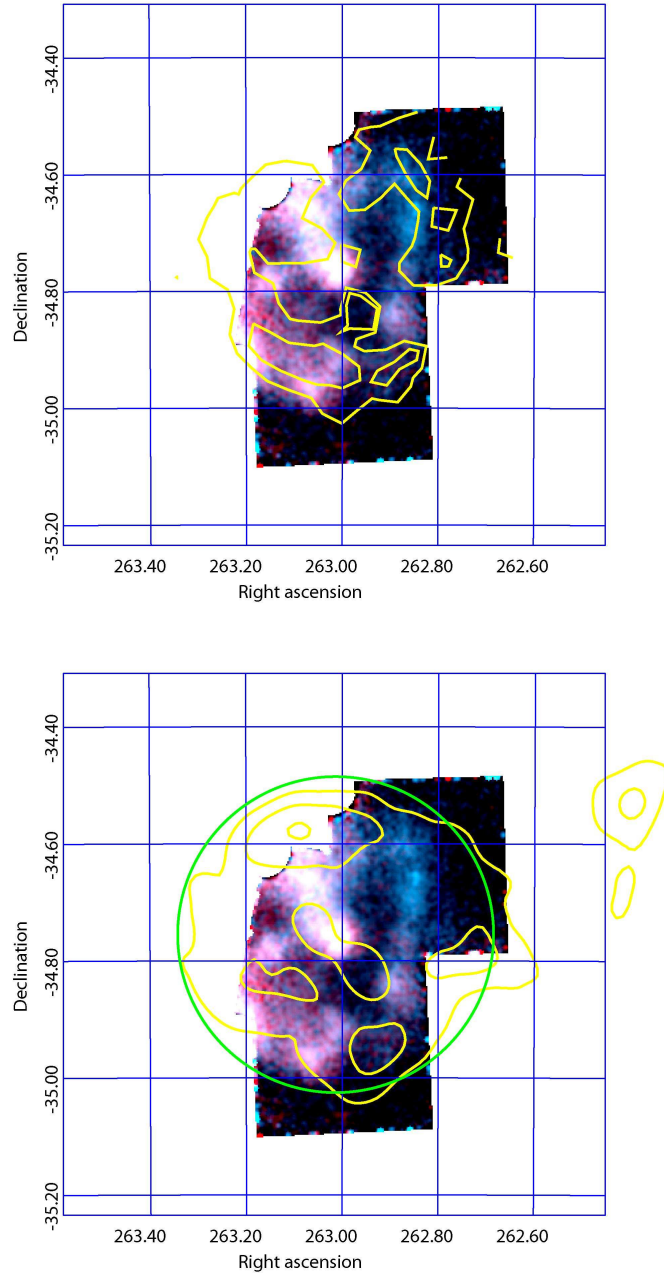


Fig. 3.— Multiwavelength view of the HESS J1731–347 region. The color images show the *Suzaku* data in a false-color representation with the same color scaling as in Fig. 2, whereas the contours are derived from the ATCA radio map at 1.4 GHz (top) and from the H.E.S.S. VHE gamma-ray excess count map (Abramowski et al. 2011) (bottom). The green circle denotes the best-fit model of the VHE shell, which has a radius of 0.27 deg. and an unresolved shell width.

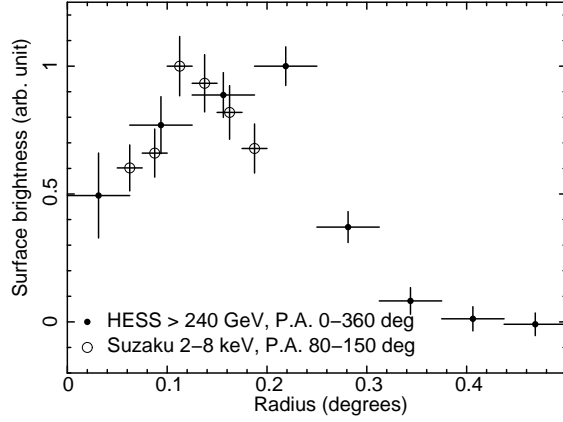


Fig. 4.— VHE  $\gamma$ -ray (filled circle) and 2–8 keV (open circle) radial profiles. Both profiles are centered on the central compact object, (RA, Dec.) = (263.0125, -34.755). The central part was cut in the X-ray data due to the contamination from the central source. Note that the VHE  $\gamma$ -ray profile is taken from the entire remnant, whereas the X-ray one is from the Western part of the shell, using position angle (P.A.)  $80^\circ$ – $150^\circ$  (counted clockwise starting from North).

Table 1. Observation Log

ObsID	Date YYYY/MM/DD	Position (J2000)	XIS Exposure [ksec]	HXD Exposure [ksec]	SCI
401099010 . . . . .	2007/02/23-24	(263.0179, -34.7706)	41	35	OFF
504031010 . . . . .	2010/02/18-19	(263.0074, -34.9458)	42	34	ON
504032010 . . . . .	2010/02/17-18	(262.8483, -34.6325)	42	33	ON

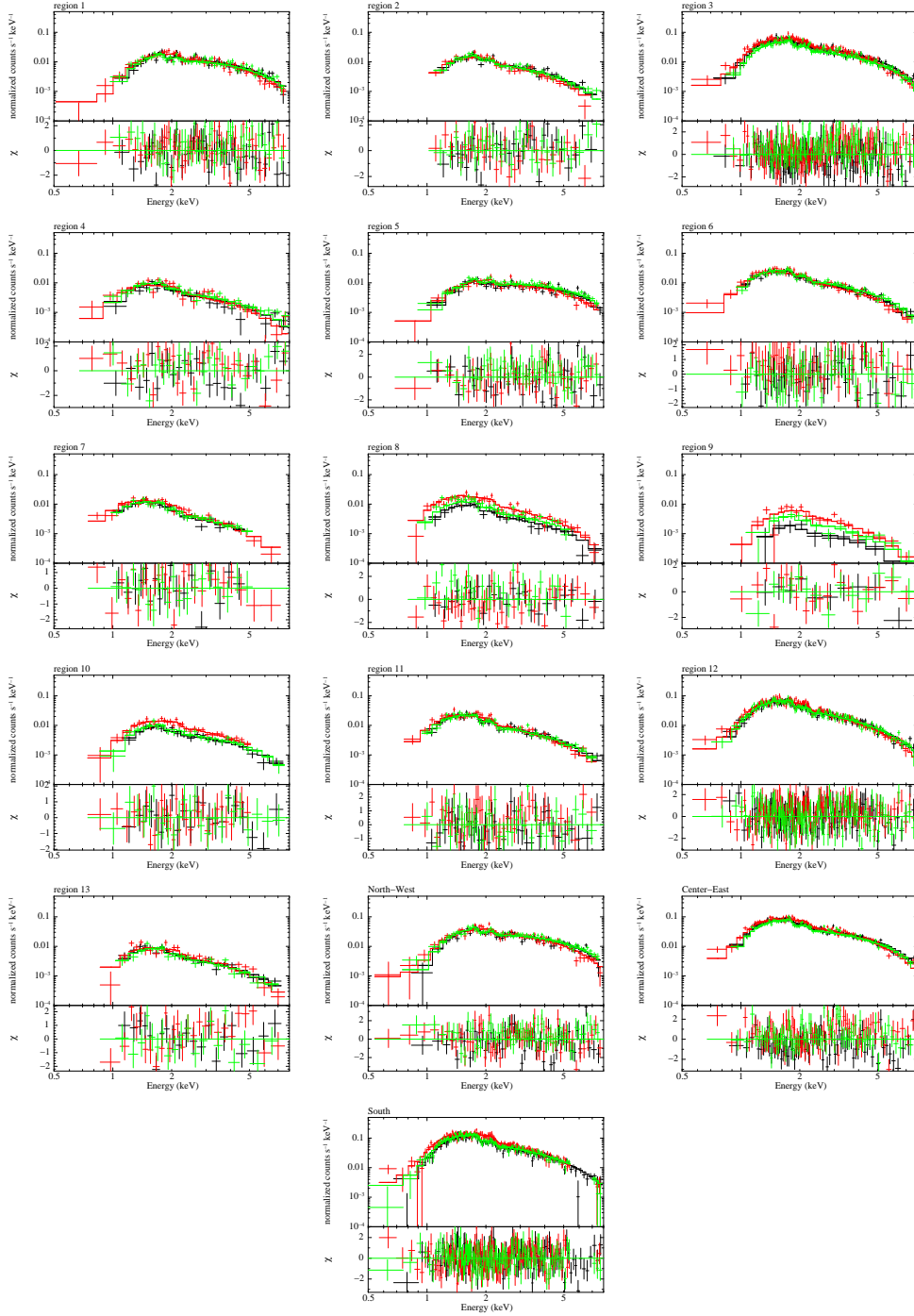


Fig. 5.— XIS spectra of each region (for the region definition see Fig. 1) and combined one (see text). The color represents XIS0 (black), XIS1 (red), and XIS3 (green). The solid lines represent the best-fit absorbed power-law model. The lower panels show the residuals from the best-fit models, respectively.

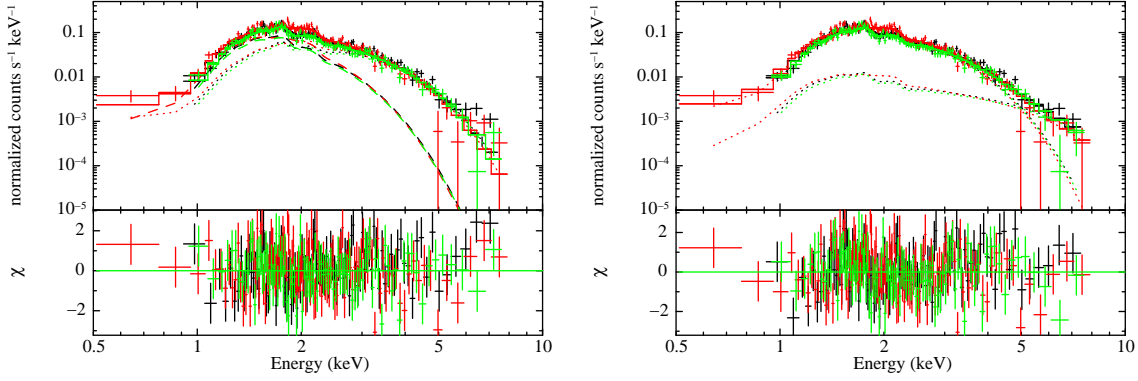


Fig. 6.— XIS spectra of XMMU J173203.3–344518. The color represents XIS0 (black), XIS1 (red), and XIS3 (green). Left panel shows the two-temperature model fitting, whereas the right one shows a single blackbody plus SNR contamination model fitting. The lower panels show the residuals from the best-fit model.

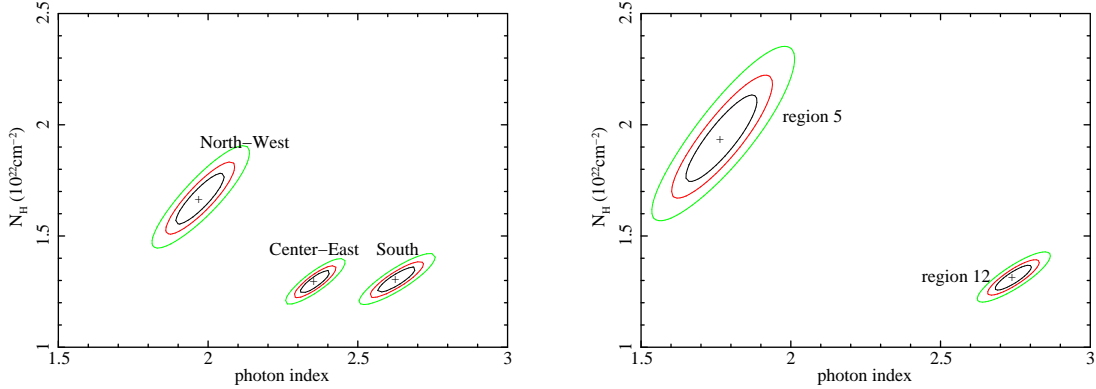


Fig. 7.— 68% (black), 90% (red), and 99% (green) confidence contours of the photon index vs. absorption column for North-West, Center-East, and South regions (left) and regions 5 and 12 (right).

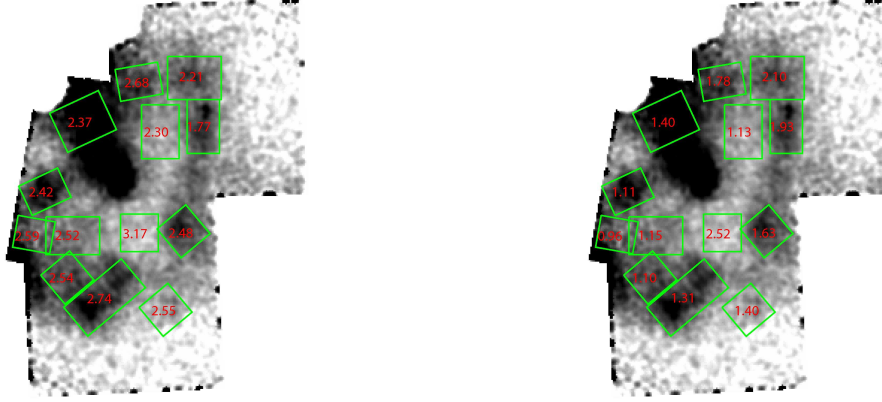


Fig. 8.— Best-fit photon index (left) and absorption column density (right) in each region.

Table 2. Best-fit parameters of spectral fittings<sup>a</sup>.

Region	$N_{\text{H}}$ ( $10^{22} \text{ cm}^{-2}$ )	$\Gamma$	$F_{2-10\text{keV}}$ ( $10^{-12} \text{ erg cm}^{-2}\text{s}^{-1}$ )	Surface brightness ( $10^{-13} \text{ erg cm}^{-2}\text{s}^{-1}\text{arcmin}^{-2}$ )	$\chi^2/\text{d.o.f.}$
1 .....	2.11 (1.92–2.30)	2.21 (2.09–2.33)	2.07 (2.00–2.15)	1.04 (1.00–1.08)	173.6/153
2 .....	1.78 (1.61–1.95)	2.68 (2.53–2.84)	1.66 (1.61–1.95)	1.38 (1.34–1.63)	98.5/93
3 .....	1.40 (1.34–1.47)	2.37 (2.31–2.43)	5.44 (5.32–5.56)	2.72 (2.66–2.78)	371.5/320
4 .....	1.12 (0.92–1.36)	2.30 (2.09–2.54)	0.73 (0.67–0.78)	0.42 (0.38–0.45)	111.7/79
5 .....	1.93 (1.73–2.15)	1.77 (1.64–1.90)	2.19 (2.10–2.27)	1.46 (1.40–1.51)	144.2/124
6 .....	1.11 (1.02–1.21)	2.42 (2.32–2.53)	2.01 (1.94–2.09)	1.68 (1.62–1.74)	137.8/136
7 .....	0.96 (0.82–1.12)	2.59 (2.38–2.81)	1.17 (1.05–1.29)	1.11 (1.00–1.23)	54.8/60
8 .....	1.15 (1.00–1.31)	2.52 (2.33–2.71)	1.54 (1.43–1.66)	0.88 (0.82–0.95)	119.0/94
9 .....	2.52 (1.96–3.18)	3.17 (2.70–3.71)	0.19 (0.13–0.24)	0.16 (0.11–0.20)	47.8/40
10 .....	1.63 (1.42–1.86)	2.48 (2.29–2.68)	1.56 (1.43–1.69)	1.27 (1.17–1.38)	49.7/74
11 .....	1.10 (1.00–1.20)	2.54 (2.43–2.66)	1.53 (1.47–1.60)	1.25 (1.20–1.31)	122.7/124
12 .....	1.31 (1.25–1.37)	2.74 (2.68–2.81)	3.20 (3.12–3.27)	1.31 (1.27–1.33)	380.4/337
13 .....	1.40 (1.18–1.65)	2.55 (2.34–2.78)	0.65 (0.60–0.70)	0.53 (0.49–0.57)	82.5/65
North-West.	1.66 (1.54–1.79)	1.97 (1.88–2.06)	4.55 (4.43–4.67)	0.86 (0.84–0.89)	240.2/180
Center-East	1.29 (1.24–1.35)	2.36 (2.30–2.41)	7.53 (7.38–7.68)	2.35 (2.31–2.40)	318.0/229
South.....	1.30 (1.24–1.36)	2.63 (2.56–2.70)	7.74 (7.50–7.98)	0.85 (0.82–0.88)	347.4/355

<sup>a</sup>Errors indicate single parameter 90% confidence regions.

Table 3. Best-fit parameters of spectral fittings of XMMU J173203.3–344518<sup>a</sup>.

Parameters	2 blackbody case	blackbody + SNR contamination
$N_{\text{H}}$ ( $10^{22}$ cm <sup>-2</sup> )	1.7 (1.5–2.0)	1.5 (1.4–1.6)
$kT_1$ (keV)	0.33 (0.26–0.42)	0.47 (0.46–0.48)
$Norm_1^{\text{b}}$	14 (12–16)	—
$kT_2$ (keV)	0.58 (0.53–0.72)	—
$Norm_2^{\text{b}}$	3.5 (0.6–7.0)	—
SNR contamination ( $10^{-13}$ erg cm <sup>-2</sup> s <sup>-1</sup> arcmin <sup>-2</sup> ) <sup>c</sup>	—	5.6 (4.2–7.0)

<sup>a</sup>Errors indicate single parameter 90% confidence regions.

<sup>b</sup> $R_{\text{km}}^2/D_{10}^2$ , where  $R_{\text{km}}$  is the source radius in km, and,  $D_{10}$  is the distance to the source in units of 10 kpc.

<sup>c</sup>2–10 keV band.